



ENERGY HARVESTING

In situ photocatalytically enhanced thermogalvanic cells for electricity and hydrogen production

Yijin Wang^{1,2}, Youzi Zhang^{1,2}, Xu Xin^{1,2}, Jiabao Yang^{1,2}, Maohuai Wang³, Ruiling Wang^{1,2}, Peng Guo^{1,2}, Wenjing Huang⁴, Ana Jorge Sobrido⁵, Bingqing Wei⁶, Xuanhua Li^{1,2,*}

High-performance thermogalvanic cells have the potential to convert thermal energy into electricity, but their effectiveness is limited by the low concentration difference of redox ions. We report an in situ photocatalytically enhanced redox reaction that generates hydrogen and oxygen to realize a continuous concentration gradient of redox ions in thermogalvanic devices. A linear relation between thermopower and hydrogen production rate was established as an essential design principle for devices. The system exhibited a thermopower of 8.2 millivolts per kelvin and a solar-to-hydrogen efficiency of up to 0.4%. A large-area generator (112 square centimeters) consisting of 36 units yielded an open-circuit voltage of 4.4 volts and a power of 20.1 milliwatts, as well 0.5 millimoles of hydrogen and 0.2 millimoles of oxygen after 6 hours of outdoor operation.

Thermal energy (heat fluxes of 0 °C to 100 °C above ambient) can come from a variety of natural and industrial processes, including solar and geothermal energy, transportation, manufacturing, electronics, and biological entities (1–4). Heat can be converted into electrical energy by using thermoelectric technologies in combination with solar illumination, but conventional thermoelectric technologies are limited by their low thermopower of microvolts per kelvin ($\mu\text{V K}^{-1}$) (5–8). Thermogalvanic and thermodiffusion cells are two alternatives that offer high thermopower of millivolts per degree (mV K^{-1}) and enable a scalable route for directly converting heat to electricity (9–11). Thermodiffusion cells based on the thermodiffusion effect of ions (ΔD) have been reported to have a considerable thermopower of 24 mV K^{-1} , but their discontinuous electrical output has made them unreliable for practical applications (12, 13). By contrast, thermogalvanic cells (TGCs) generate continuous electric power by operating under a temperature difference (ΔT), which hold promise for practical applications (14). Previous studies have reported a thermopower of 3.7 mV K^{-1} and a normalized power density ($P_{\text{max}}/\Delta T^2$) of 6.8 $\text{mW m}^{-2} \text{K}^{-2}$, obtained from the heat provided by an ideal laboratory heater and cooler plates (1), whereas a thermopower of 1.3 mV K^{-1} and a $P_{\text{max}}/\Delta T^2$ of 0.03 $\text{mW m}^{-2} \text{K}^{-2}$ was ob-

tained with solar thermal energy devices (15). We report an in situ-enhanced thermopower of 8.2 mV K^{-1} and a $P_{\text{max}}/\Delta T^2$ of 8.5 $\text{mW m}^{-2} \text{K}^{-2}$ in a TGC (3.14 cm^2) for harvesting solar thermal energy by using a photocatalytic water splitting process with simultaneous hydrogen (H_2 , 11.3 $\mu\text{mol hour}^{-1}$) and stoichiometric oxygen production (O_2 , 5.5 $\mu\text{mol hour}^{-1}$).

Thermopower is associated with the solvent-dependent entropy difference (ΔS) between redox ions and the concentration difference (ΔC) of redox ions between hot and cold sides (2, 16, 17). Thermopower can be enhanced by increasing ΔS of the redox ions. For example, a polymer network bonded with ferrocyanide (FeCN^{4-}) increased ΔS to achieve a thermopower of 1.7 mV K^{-1} (18). Introducing the acrylic quaternary ammonium monomer into the $\text{Fe}^{3+}/\text{Fe}^{2+}$ electrolyte to adjust the redox couple's solvation shells led to a larger ΔS with an enhanced thermopower of 2.0 mV K^{-1} (19). However, owing to the spontaneous diffusion of redox ions into a homogeneous state, the ΔC of these TGCs is thermodynamically unstable and decreases to near zero (Fig. 1A) (20–22). Guanidinium cations can selectively induce the crystallization of FeCN^{4-} ions and improve the ΔC between hot and cold sides while leaving the concentration of ferricyanide (FeCN^{3-}) unchanged on both hot and cold sides. This approach resulted in a limited ΔC and poor thermopower of 3.7 mV K^{-1} (1). Therefore, the construction of a high and continuous ΔC for both redox ions between the hot and cold sides and interpretation of the intrinsic ΔC modulation mechanism constitute a tremendous challenge.

We report the design of an in situ photocatalytically enhanced thermogalvanic device that can boost the thermopower to 8.2 mV K^{-1} and provide solar-to-hydrogen (STH) efficiency of up to 0.4% (Fig. 1B). An O_2 -evolution photocatalyst (OEP) aided the forward reaction from FeCN^{3-} to FeCN^{4-} and facilitated H_2O to O_2 production (23), resulting in a high FeCN^{4-} con-

centration on the hot side. The H_2 -evolution photocatalyst (HEP) converted the FeCN^{4-} to FeCN^{3-} and facilitated H_2 production from H_2O (24), increasing the amount of FeCN^{3-} on the cold side. A high local concentration of FeCN^{4-} near the hot side thermodynamically enhanced the oxidation reaction $\text{FeCN}^{4-} \rightarrow \text{FeCN}^{3-} + e^-$ with more electrons transferred to the hot electrode, whereas a high local concentration of FeCN^{3-} near the cold side thermodynamically enhanced the reduction reaction $\text{FeCN}^{3-} + e^- \rightarrow \text{FeCN}^{4-}$ with more electrons attracted from the cold electrode, enabling a continuous reaction to produce a high voltage. As the photocatalytic reaction proceeded, a H^+ concentration gradient was also formed within the system. Thus, the thermopower of the photocatalytically enhanced TGC was further increased by enhancing ΔC of FeCN^{4-} , FeCN^{3-} , and H^+ along with the improved ΔS .

Cell fabrication and ΔC construction

We constructed an integrated system using a multistep polymerization method (Fig. 1C; see the Experiments section for details). Polyacrylic acid (PAA) was chosen as the matrix given its simple synthesis and low cost and was filled with water to ensure ion migration and photocatalytic reaction. We then added $\text{FeCN}^{4-/3-}$ to the PAA precursor to serve as redox ions for the thermogalvanic reaction. Oxygen vacancies in WO_3 photocatalysts ($\text{O}_v\text{-WO}_3$) with CoO_x and sulfur vacancies in ZnIn_2S_4 photocatalysts ($\text{S}_v\text{-ZIS}$) with Pt were introduced into the upper and lower layers of the PAA precursor, respectively, to serve as an OEP and HEP, respectively (Fig. 1, D and E). The introduction of vacancies in the photocatalysts can enhance the charge transport and improve the photocatalytic efficiency (fig. S1, E and F), which is consistent with our previous report (25). CoO_x as an oxygen production cocatalyst, was predeposited on the surfaces of $\text{O}_v\text{-WO}_3$ by a calcination method, whereas Pt, as a hydrogen production cocatalyst, was predeposited on the surfaces of $\text{S}_v\text{-ZIS}$ by a reduction method. Cocatalysts can increase the driving force for extracting carriers and provide photocatalytic active sites to boost the photocatalytic efficiency (fig. S1, E and F) (26). The pristine TGC was hereafter assigned to the PAA- $\text{FeCN}^{4-/3-}$ complex. After $\text{O}_v\text{-WO}_3$ with CoO_x and $\text{S}_v\text{-ZIS}$ with Pt were introduced into the TGC, we referred to the cell as the $\text{O}_v\text{-WO}_3/\text{TGC}/\text{S}_v\text{-ZIS}$ system. Scanning electron microscopy (SEM) and transmission electron microscopy (TEM) were used to verify that the $\text{O}_v\text{-WO}_3/\text{TGC}/\text{S}_v\text{-ZIS}$ system was successfully constructed (fig. S2), and Raman spectroscopy data suggested that $\text{FeCN}^{4-/3-}$ was evenly distributed throughout the system. The depth of distribution for $\text{O}_v\text{-WO}_3$ and $\text{S}_v\text{-ZIS}$ in the $\text{O}_v\text{-WO}_3/\text{TGC}/\text{S}_v\text{-ZIS}$ system was 1 to 3 mm and 7 to 9 mm, respectively (fig. S3).

¹State Key Laboratory of Solidification Processing, Center for Nano Energy Materials, School of Materials Science and Engineering, Northwestern Polytechnical University, Xi'an 710072, P. R. China. ²Research and Development Institute of Northwestern Polytechnical University, Shenzhen 518057, P. R. China. ³Department of Materials Science and Engineering, City University of Hong Kong, Hong Kong SAR, P. R. China. ⁴School of Materials Science and Engineering, Nanyang Technological University, Singapore 639798, Singapore. ⁵School of Engineering and Materials Science, Faculty of Science and Engineering, Queen Mary University of London, Mile End Road, London E1 4NS, UK. ⁶Department of Mechanical Engineering, University of Delaware, Newark, DE 19716, USA.

*Corresponding author. Email: lixh32@nwpu.edu.cn

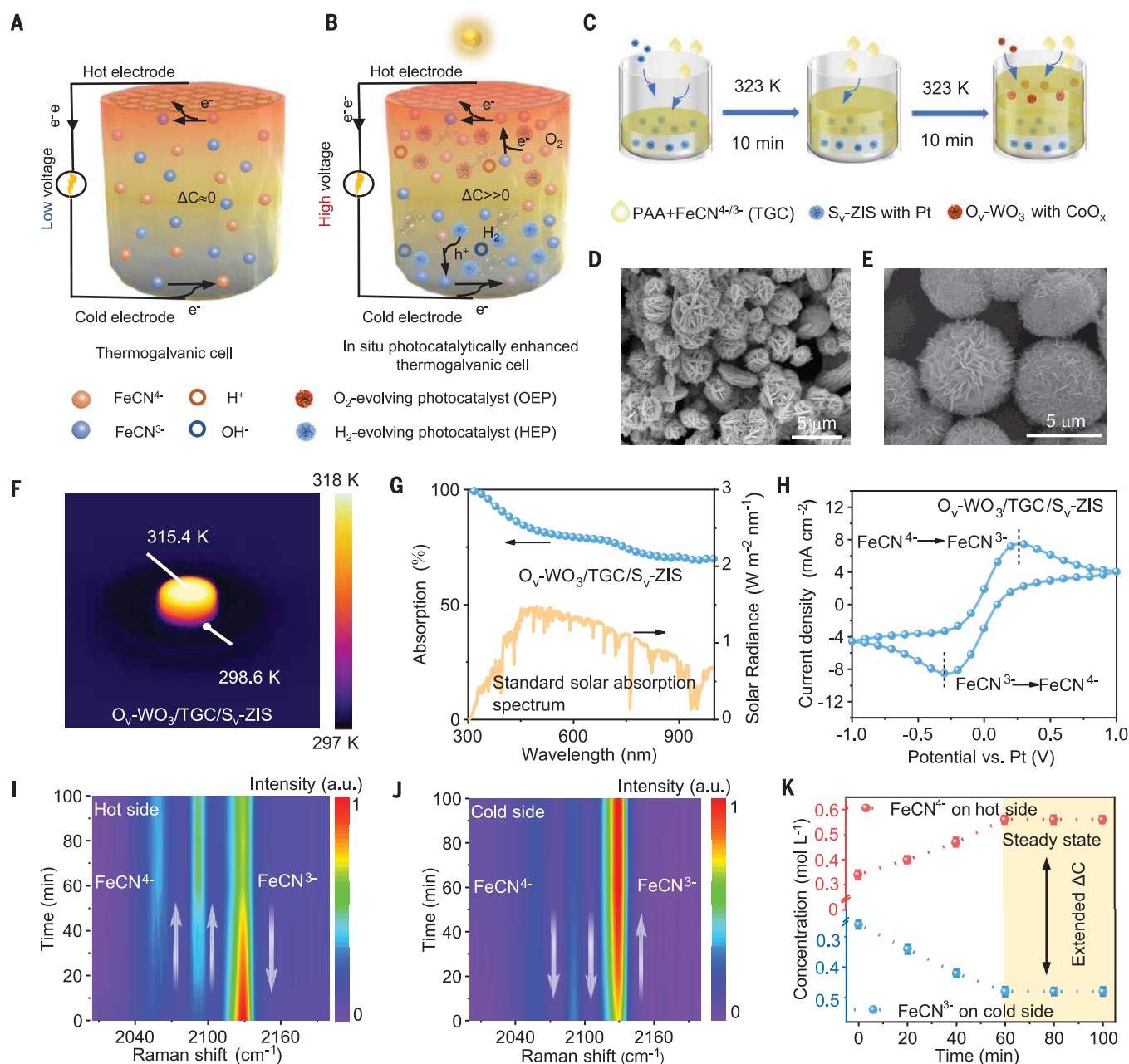


Fig. 1. In situ photocatalytically enhanced concentration gradient of redox ions in a TGC. (A and B) Schematic depiction of the thermogalvanic cell (TGC) and photocatalytically enhanced TGC. (C) Schematic illustration of the fabrication for the $O_V\text{-WO}_3/\text{TGC}/S_V\text{-ZIS}$ system. FeCN^{4-} and FeCN^{3-} concentrations were 0.34 M and 0.26 M, respectively. (D and E) SEM images of (D) $O_V\text{-WO}_3$ with CoO_x and (E) $S_V\text{-ZIS}$ with Pt. (F) Infrared thermal image of the $O_V\text{-WO}_3/\text{TGC}/S_V\text{-ZIS}$ under 100 mW cm^{-2} light irradiation at a 30° angle. (The

cold side was controlled at 298 K.) TGC denoted $\text{PAA-FeCN}^{4-/3-}$. (G) Absorption spectrum of the $O_V\text{-WO}_3/\text{TGC}/S_V\text{-ZIS}$. (H) Cyclic voltammetry (CV) curve of the $O_V\text{-WO}_3/\text{TGC}/S_V\text{-ZIS}$. (I and J) Real-time monitoring of $\text{FeCN}^{4-/3-}$ through in situ Raman study for the hot and cold sides of the $O_V\text{-WO}_3/\text{TGC}/S_V\text{-ZIS}$ under light irradiation (100 mW cm^{-2}). (K) Time courses of FeCN^{4-} and FeCN^{3-} concentrations on the hot and cold sides of $O_V\text{-WO}_3/\text{TGC}/S_V\text{-ZIS}$ under light irradiation (100 mW cm^{-2}). Error bars represent the standard deviation of 10 repeated measurements.

We investigated ΔT by placing the system in water under light irradiation. The top of the $O_V\text{-WO}_3/\text{TGC}/S_V\text{-ZIS}$ system absorbed light that was converted to heat, which created a 16.8 K temperature gradient (Fig. 1F). The $O_V\text{-WO}_3/\text{TGC}/S_V\text{-ZIS}$ system exhibited high light absorbance within the wavelength range of 300

to 1000 nm, which ensured that the photocatalytic process took place (Fig. 1G). Two redox peaks in the potential window of -0.28 to 0.28 V (versus Pt) were observed in the cyclic voltammetry curve that were attributed to the reduction of FeCN^{3-} to FeCN^{4-} and the oxidation of FeCN^{4-} to FeCN^{3-} , respectively (I2), confirm-

ing the continuous thermoelectric and photocatalytic reactions (Fig. 1H).

In situ Raman spectroscopy was used to monitor real-time changes in FeCN^{3-} and FeCN^{4-} concentrations for the $O_V\text{-WO}_3/\text{TGC}/S_V\text{-ZIS}$ system under light irradiation (fig. S4) (27). Peaks observed at 2058 and 2091 cm^{-1} were attributed

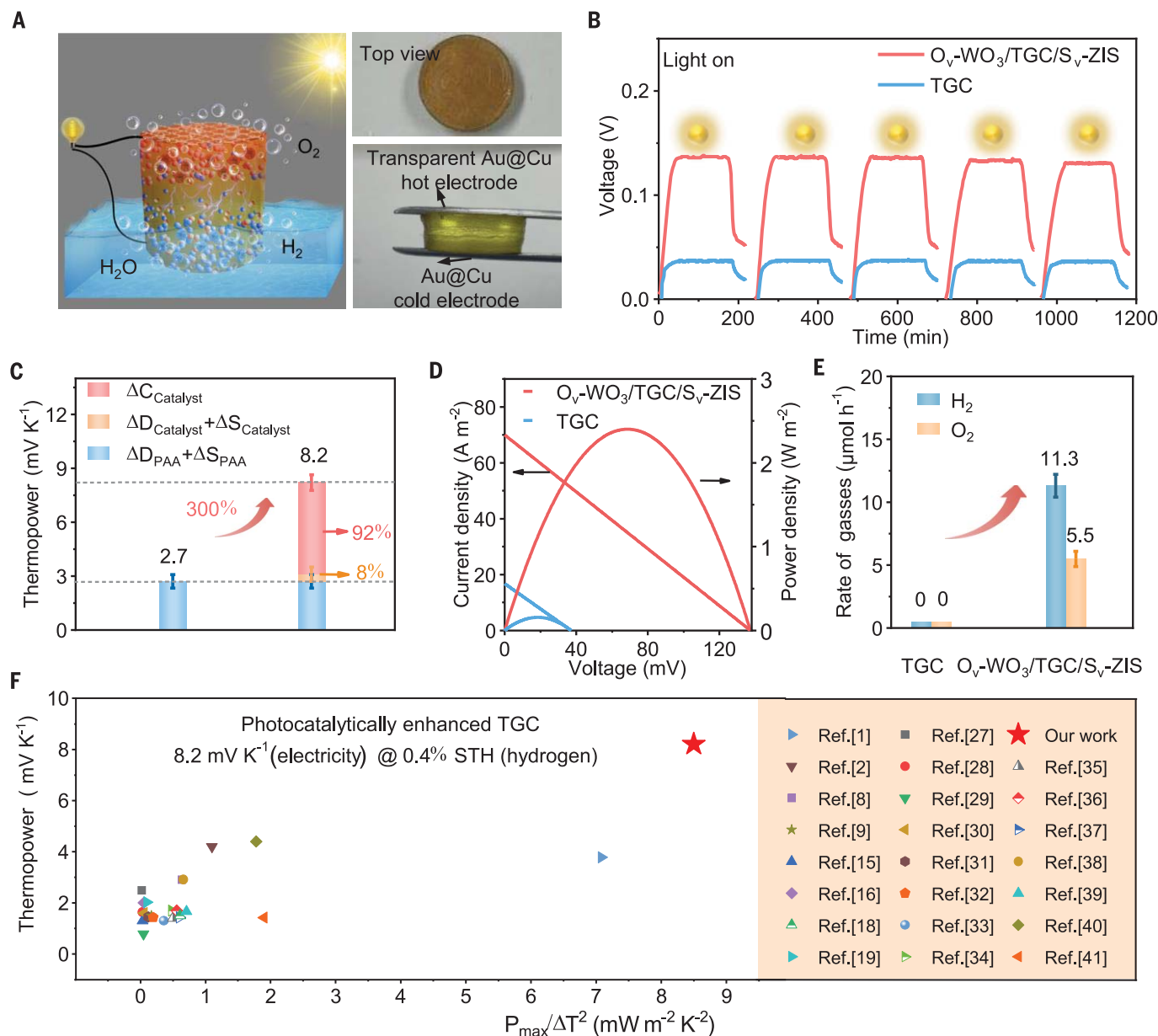


Fig. 2. Thermoelectric performances of the TGC and O_v-WO₃/TGC/S_v-ZIS.

(A) Schematic diagram of the photocatalytically enhanced TGC under light irradiation. The cross-sectional area of the cell was 3.14 cm² with a radius of 1 cm. The distance between the two electrodes was 0.9 cm (upper electrode: transparent Au@Cu mesh; bottom electrode: Au@Cu foil). (B) V_{OC} response versus time curves of TGC and O_v-WO₃/TGC/S_v-ZIS for five cycles (reaction condition: 2 ml of pure water, 100 mW cm⁻² light irradiation). (C) Thermopowers of TGC and O_v-WO₃/

TGC/S_v-ZIS (relative contributions of ΔD+ΔS and ΔC with photocatalysts to the enhanced thermopower). (D) Current-voltage curves and corresponding power densities of TGC (ΔT = 13.8 K) and O_v-WO₃/TGC/S_v-ZIS (ΔT = 16.8 K). (E) Hydrogen and oxygen evolution rates of TGC and O_v-WO₃/TGC/S_v-ZIS (reaction conditions: 3 mg of O_v-WO₃, 2.5 mg of S_v-ZIS, 100 mW cm⁻² light irradiation). (F) Comparison of the thermopower and normalized power density values for various TGCs (table S2). Error bars in (C) and (E) represent the standard deviation of 10 repeated measurements.

to the A_g and E_g modes of FeCN⁴⁻, respectively. An additional peak located at 2128 cm⁻¹ was observed, corresponding to FeCN³⁻ (Fig. 1I). Under light irradiation, the characteristic peak intensities of FeCN³⁻ and FeCN⁴⁻ on both sides of the TGC without photocatalysts remained unchanged. On the hot side of the O_v-WO₃/TGC/S_v-ZIS system, with the aid of photocatalysts, the peak intensities of FeCN⁴⁻ and FeCN³⁻ gradually increased and decreased, respectively, with

an increase in the illumination time. This observation indicated that the O_v-WO₃ photocatalysts converted FeCN³⁻ to FeCN⁴⁻ on the hot side. The peak intensities remained constant after 60 min, indicating that the distribution of FeCN³⁻ and FeCN⁴⁻ had reached a steady state. Similarly, on the cold side, the S_v-ZIS photocatalysts caused FeCN³⁻ peak intensities to gradually increase and FeCN⁴⁻ peak intensities to gradually decrease for up

to 60 min (Fig. 1J). Ultraviolet-visible (UV-vis) absorption spectroscopy was used to measure the concentration changes during the time course of illumination (Fig. 1K and fig. S5) (I). The result showed that after 60 min of illumination, the ΔC of FeCN⁴⁻ and FeCN³⁻ between hot and cold sides was 0.44 mol liter⁻¹, and pH measurements showed a ΔC of H⁺ of 3.3 × 10⁻⁷ mol liter⁻¹ between hot and cold sides of the system (fig. S6).

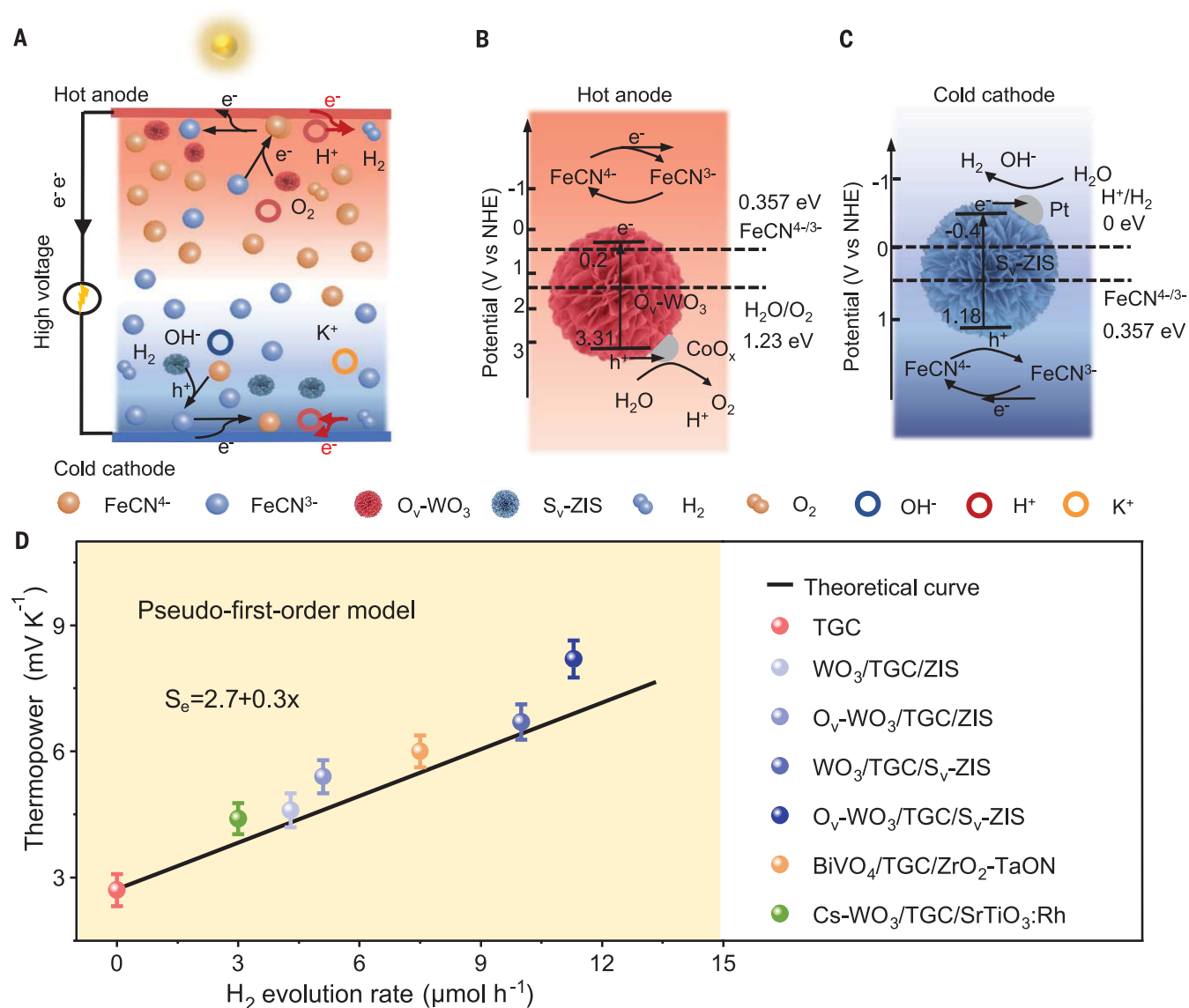


Fig. 3. Validating the working principle of photocatalytically enhanced TGCs. (A) Schematic of the photocatalytically enhanced TGC of $O_v\text{-WO}_3/\text{TGC}/S_v\text{-ZIS}$. (B and C) Working principle of photocatalytically enhanced TGCs of $O_v\text{-WO}_3/\text{TGC}/S_v\text{-ZIS}$: (B) hot side and (C) cold side. (D) Relationship of thermopower and H_2 evolution rate in the photocatalytically enhanced TGCs. Error bars represent the standard deviation of 10 repeated measurements.

Thermoelectric performance

We evaluated the thermoelectric performance of TGC and $O_v\text{-WO}_3/\text{TGC}/S_v\text{-ZIS}$ by using a Au-coated Cu (Au@Cu) mesh with 91% transmittance as a transparent hot electrode and a Au@Cu foil as the cold electrode (Fig. 2A and fig. S7). When exposed to light irradiation (100 mW cm^{-2}), the TGC and $O_v\text{-WO}_3/\text{TGC}/S_v\text{-ZIS}$ showed ΔT of 13.8 and 16.8 K, respectively (fig. S8). The open-circuit voltage (V_{oc}) on the $O_v\text{-WO}_3/\text{TGC}/S_v\text{-ZIS}$ achieved 137 mV, much higher than that of TGC of only 37 mV (fig. S9). The V_{oc} of the $O_v\text{-WO}_3/\text{TGC}/S_v\text{-ZIS}$ system was 131 mV after five cycles (Fig. 2B and fig. S10). Moreover, the thermopower (i.e., $\Delta V/\Delta T$) of $O_v\text{-WO}_3/\text{TGC}/S_v\text{-ZIS}$, driven by ΔD (the thermodiffusion effect of K^+ , $\text{FeCN}^{4-/3-}$, and H^+),

ΔS (the enhanced solvent-dependent entropy difference of $\text{FeCN}^{3-}/\text{FeCN}^{4-}$ and H^+/H_2), and ΔC (the concentration difference of FeCN^{3-} , FeCN^{4-} , and H^+ between cold and hot sides), was 8.2 mV K^{-1} and 3.0 times as high as that of TGC (2.7 mV K^{-1}), which was driven only by ΔD and ΔS contributions (18) (Fig. 2C and supplementary note S1). For $O_v\text{-WO}_3/\text{TGC}/S_v\text{-ZIS}$, only 8% of the enhanced thermopower was contributed by ΔD and ΔS versus 92% by ΔC (figs. S11 and S12 and table S1). The optimized amounts of FeCN^{3-} , FeCN^{4-} , $O_v\text{-WO}_3$, and $S_v\text{-ZIS}$ that resulted in the largest V_{oc} values were $0.26 \text{ mol liter}^{-1}$, $0.34 \text{ mol liter}^{-1}$, 3 mg, and 2.5 mg, respectively (fig. S13). The thermopower and light intensity were positively correlated (fig. S14). The thermopower

was also dependent on the location of the photocatalysts (fig. S15).

The short-circuit current density, the maximum power density (P_{max}), and the normalized power density ($P_{max}/\Delta T^2$) of $O_v\text{-WO}_3/\text{TGC}/S_v\text{-ZIS}$ were $\sim 70 \text{ A m}^{-2}$, 2398 mW m^{-2} , and $8.5 \text{ mW m}^{-2} \text{ K}^{-2}$, respectively (Fig. 2D). Furthermore, the figures of merit (ZT) and Carnot-relative efficiency (η_c) for $O_v\text{-WO}_3/\text{TGC}/S_v\text{-ZIS}$ were calculated to be 0.17 and 4.91%, respectively, whereas the values for TGC were much lower, at 0.02 and 0.47%, respectively. The thermal and electrical conductivities of the systems with and without catalysts were unchanged (fig. S16). The H_2 and O_2 photoproduction rates of the $O_v\text{-WO}_3/\text{TGC}/S_v\text{-ZIS}$ system were 11.3 and $5.5 \mu\text{mol hour}^{-1}$, respectively (Fig. 2E).

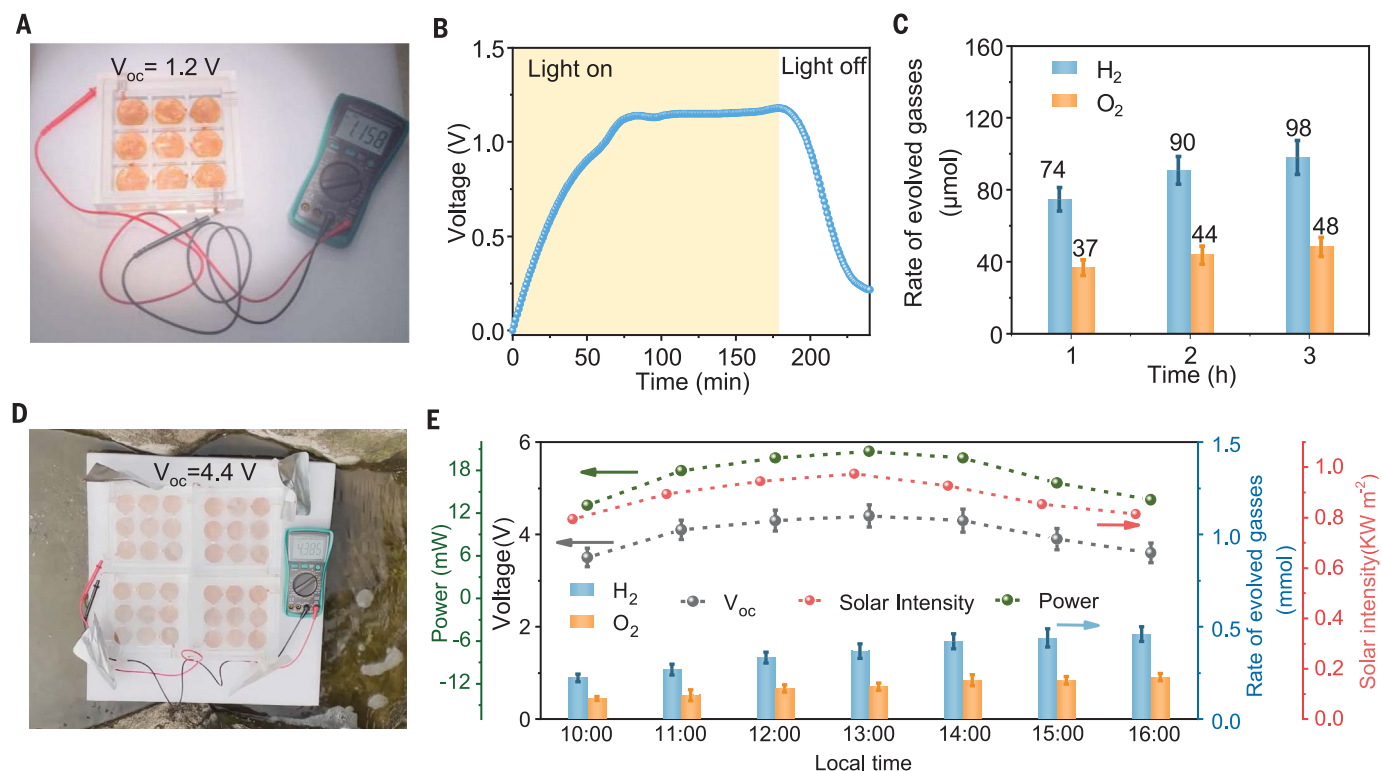


Fig. 4. A large-area photocatalytically enhanced TGC. (A) Schematic drawing of a large-area photocatalytically enhanced thermogalvanic device with nine units in series (28 cm^2). (B and C) (B) Voltage generated and (C) amount of evolved gases from a large-area photocatalytically enhanced thermogalvanic device with nine units in series (28 cm^2) under light illumination (reaction conditions: 27 mg of $\text{O}_v\text{-WO}_3$, 22.5 mg of $\text{S}_v\text{-ZIS}$, 18 ml of pure water, 100 mW cm^{-2} light irradiation). Error bars indicate the standard deviation of three measurements. (D) Schematic drawing of a large-area photocatalytically enhanced

thermogalvanic device with 36 units in series (112 cm^2) under the natural sunlight condition. (E) Voltage (black), power (green), solar intensity (red), and amount of evolved gases for a large-area photocatalytically enhanced thermogalvanic device with 36 units in series (112 cm^2) under the natural sunlight condition from 10:00 to 16:00 (7 July 2022) at Northwestern Polytechnical University of Xi'an (reaction conditions: 108 mg $\text{O}_v\text{-WO}_3$, 90 mg of $\text{S}_v\text{-ZIS}$, 72 ml of pure water). Error bars indicate the standard deviation of the three independent measurements on the same date.

^{18}O isotope-labeled photocatalytic measurements demonstrated that the detected O_2 was the product of water splitting (figs. S17 and S18).

The $\text{O}_v\text{-WO}_3/\text{TGC}/\text{S}_v\text{-ZIS}$ system demonstrated a photocatalytically enhanced thermopower of 8.2 mV K^{-1} versus that of other reported TGCs (Fig. 2F and table S2) (1, 2, 8, 9, 15, 16, 18, 19, 28–42). The normalized power density of $8.5 \text{ mW m}^{-2} \text{ K}^{-2}$ also exceeded that of other TGCs. The STH energy conversion efficiency was 0.4% (table S3), comparable to that of other reported photocatalysts with aqueous redox mediators (table S4).

Validating the working principle

A working principle for this photocatalytically enhanced thermopower of the system was proposed (Fig. 3A). The band structures for the $\text{O}_v\text{-WO}_3$ and $\text{S}_v\text{-ZIS}$ photocatalysts were determined using UV-vis diffuse reflectance spectroscopy and UV photoelectron spectra (fig. S19). Under light illumination, photogenerated electrons with sufficient energy were excited from the valence band maximum (VBM) of $\text{O}_v\text{-WO}_3$ and $\text{S}_v\text{-ZIS}$ to the conduction band minimum (CBM) of $\text{O}_v\text{-WO}_3$ and $\text{S}_v\text{-ZIS}$, respectively, and holes were generated on the

VBM of $\text{O}_v\text{-WO}_3$ and $\text{S}_v\text{-ZIS}$ (Fig. 3, B and C). The electrons in the CBM of $\text{O}_v\text{-WO}_3$ on the hot side facilitated the forward reaction from FeCN^{3-} to FeCN^{4-} because the CBM of $\text{O}_v\text{-WO}_3$ was higher than the redox potential of $\text{FeCN}^{4-/3-}$, resulting in a high concentration of FeCN^{4-} ions (Fig. 3B). The band alignment of $\text{O}_v\text{-WO}_3$ and CoO_x cocatalysts allowed holes to be efficiently extracted from the VBM of $\text{O}_v\text{-WO}_3$ to CoO_x cocatalysts through the built-in electric field at the interface, which drove oxygen production (figs. S19 and S20). On the cold side, the holes in the VBM of $\text{S}_v\text{-ZIS}$ increased the amount of FeCN^{3-} ions by converting FeCN^{4-} to FeCN^{3-} ions (the VBM of $\text{S}_v\text{-ZIS}$ was lower than the redox potential of $\text{FeCN}^{4-/3-}$) (Fig. 3C). The Pt cocatalysts served as an electron trap and attracted electrons from the CBM of $\text{S}_v\text{-ZIS}$ through a Schottky junction (Pt/ $\text{S}_v\text{-ZIS}$) and substantially facilitated H_2 production (figs. S19 and S20). As the O_2 and H_2 evolution reactions proceeded, H^+ and OH^- were generated on the hot and cold sides of the system, respectively (Fig. 3, B and C). Because of the protonation and deprotonation processes in the PAA matrix and the H^+ thermodiffusion,

only a small ΔC of H^+ occurred between the hot and cold sides of the system (fig. S21 and supplementary note S2).

A thermogalvanic reaction also occurred in the system (Fig. 3A). Because FeCN^{4-} ions have a higher charge density and can form a more condensed hydration shell, they exhibited lower thermodynamic entropy compared with FeCN^{3-} ions (2). When a temperature gradient of 16.8 K was formed under light illumination, the high local concentration of FeCN^{4-} near the hot electrode thermodynamically enhanced the oxidation reaction $\text{FeCN}^{4-} \rightarrow \text{FeCN}^{3-} + e^-$ and resulted in the transfer of more electrons to the hot electrode (Fig. 3B). Similarly, the high local concentration of FeCN^{3-} near the cold electrode thermodynamically enhanced the reduction reaction $\text{FeCN}^{3-} + e^- \rightarrow \text{FeCN}^{4-}$ and attracted more electrons from the cold electrode (Fig. 3C). This continuous reaction facilitated the generation of a high voltage. The concentration gradient of H^+ that formed within the system had an opposing effect on the increase in thermopower of $\text{FeCN}^{4-/3-}$ (Fig. 3A). Because of its small ΔC , the contribution of H^+ was much less than that of $\text{FeCN}^{4-/3-}$ (figs.

S11 and S12). Therefore, the high local concentration of FeCN^{4-} and FeCN^{3-} (i.e., extended ΔC) induced by photocatalytic reaction supported the increased thermopower of $\text{O}_v\text{-WO}_3/\text{TGC}/\text{S}_v\text{-ZIS}$. By coupling the ΔD , ΔS , and ΔC of FeCN^{4-} and FeCN^{3-} , the high thermopower of the system was achieved.

On the basis of the above work principle and the Nernst equation between the thermopower and redox concentration (15), a universal theoretical function relation between thermopower (S_e) and H_2 production rate (x) could be established for photocatalytically enhanced TGCs (supplementary note S3)

$$S_e = S_{AD} + S_{AS}^{\text{FeCN}^{4-/3-}} + \frac{R}{nF} \left(\ln C_0^{\text{FeCN}^{4-}} - \ln C_0^{\text{FeCN}^{3-}} \right) + \frac{2R}{nF\Delta T} (T_{\text{hot}} + T_{\text{cold}}) \left(\frac{1}{C_0^{\text{FeCN}^{4-}} V_c} + \frac{1}{C_0^{\text{FeCN}^{3-}} V_c} \right) x + S_e^{\text{H}^+} \quad (1)$$

where S_{AD} is the thermodiffusion thermopower of mobile ions (i.e., K^+ , $\text{FeCN}^{4-/3-}$, H^+) and $S_{AS}^{\text{FeCN}^{4-/3-}}$ is the thermopower driven by only ΔS of FeCN^{4-} and FeCN^{3-} . $S_e^{\text{H}^+}$ is thermopower driven by the H^+ concentration gradient. V_c is the volume of the electrolyte solution of the hydrogen-evolution photocatalyst. $C_0^{\text{FeCN}^{4-}}$ and $C_0^{\text{FeCN}^{3-}}$ are the initial concentrations of FeCN^{4-} and FeCN^{3-} , respectively. F , n , and R are the Faraday constant, the number of electrons transferred during a redox reaction, and the ideal gas constant, respectively, and T_{hot} and T_{cold} are the temperatures of the hot and cold electrodes, respectively. These results showed a linear relation between the thermopower and H_2 evolution rate.

In our photocatalytically enhanced thermogalvanic system, Eq. 2 was derived from Eq. 1 by substituting the corresponding experimental parameter values (fig. S22)

$$S_e = 2.7 + 0.3x \quad (2)$$

To validate the formula's universality, a series of alternative photocatalysts with different photocatalytic properties, including $\text{BiVO}_4/\text{TGC}/\text{ZrO}_2\text{-TaON}$ and $\text{Cs-WO}_3/\text{TGC}/\text{SrTiO}_3/\text{Rh}$, were measured under the same experimental parameters in terms of thermopowers and H_2 evolution rates (fig. S23). Along with the enhanced H_2 production rates, their thermopowers revealed the linear increase and conformed to Eq. 2 (Fig. 3D). These results convincingly proved the universality of our strategy to serve as essential design principles for photocatalytically enhanced thermogalvanic devices.

Large-area thermogalvanic devices

A large prototype module (28 cm^2) containing nine units with a series connection was prepared that could reach a maximum V_{oc} of 1.2 V under 100 mW cm^{-2} light irradiation (Fig. 4, A and B). After 3 hours of irradiation, H_2 and O_2 production reached 98 and 48 μmol , re-

spectively (Fig. 4C). Outdoor experiments with the device were performed under natural sunlight. An array of the $\text{O}_v\text{-WO}_3/\text{TGC}/\text{S}_v\text{-ZIS}$ modules, with an area of 112 cm^2 , was assembled with 36 units in series that self-floated on flowing water (Fig. 4D). The natural sunlight presented a time-dependent variability in solar intensity and ambient temperature from 10:00 (the system reached a relatively stable state at this time) to 16:00 (Xi'an, 7 July 2022) (fig. S24). A V_{oc} value of 4.4 V and a power value of 20.1 mW were generated, indicating the practical application of the photocatalytically enhanced thermogalvanic technology (movie S1). After 6 hours of reaction, 0.5 mmol of H_2 and 0.2 mmol of O_2 were collected (Fig. 4E). The prototype system demonstrated a practical and sustainable way to generate electricity with H_2 and O_2 production simultaneously.

Conclusion

The photocatalytically enhanced thermogalvanic devices were demonstrated through an in situ-induced photocatalytic process that produced a continuous concentration gradient ΔC of FeCN^{4-} and FeCN^{3-} ions on both hot and cold sides. The system displayed a photocatalytically enhanced thermopower of 8.2 mV K^{-1} accompanied by simultaneous solar-driven water splitting with an STH efficiency of up to 0.4%. This pioneering system combines electricity generation with H_2 and O_2 production by harnessing energy from solar radiation. This work has also demonstrated the viability of the technology at a larger scale and under natural conditions, making it a promising method for diverse environmental energy conversion using solar-thermal energy.

REFERENCES AND NOTES

1. B. Yu *et al.*, *Science* **370**, 342–346 (2020).
2. J. Duan *et al.*, *Nat. Commun.* **9**, 5146–5153 (2018).
3. K. Chen *et al.*, *Science* **367**, 555–559 (2020).
4. S. Ohno *et al.*, *Joule* **2**, 141–154 (2018).
5. H. Wang *et al.*, *Adv. Energy Mater.* **11**, 2100481–2100486 (2021).
6. D. Kraemer *et al.*, *Nat. Energy* **1**, 16153–16160 (2016).
7. Y. Li *et al.*, *Adv. Energy Mater.* **12**, 2103666–2103675 (2022).
8. T. Kim *et al.*, *Nano Energy* **31**, 160–167 (2017).
9. W. Gao, Z. Lei, W. Chen, Y. Chen, *ACS Nano* **16**, 8347–8357 (2022).
10. Y. Liu *et al.*, *Energy Environ. Sci.* **15**, 3670–3687 (2022).
11. Y. Zheng *et al.*, *Chem. Soc. Rev.* **50**, 9022–9054 (2021).
12. C. G. Han *et al.*, *Science* **368**, 1091–1098 (2020).
13. T. Li *et al.*, *Nat. Mater.* **18**, 608–613 (2019).
14. Y. Han, J. Zhang, R. Hu, D. Xu, *Sci. Adv.* **8**, eabl5318 (2022).
15. J. Shen *et al.*, *J. Mater. Chem. A Mater. Energy Sustain.* **10**, 7785–7791 (2022).
16. H. Zhou, T. Yamada, N. Kimizuka, *J. Am. Chem. Soc.* **138**, 10502–10507 (2016).
17. M. Li, M. Hong, M. Dargusch, J. Zou, Z.-G. Chen, *Trends Chem.* **3**, 561–574 (2021).
18. Z. Lei, W. Gao, P. Wu, *Joule* **5**, 2211–2222 (2021).
19. W. Gao, Z. Lei, C. Zhang, X. Liu, Y. Chen, *Adv. Funct. Mater.* **31**, 2104071–2104078 (2021).

20. T. Ding *et al.*, *Adv. Energy Mater.* **11**, 2102219–2102227 (2021).
21. Y. Liu *et al.*, *Adv. Sci. (Weinh.)* **8**, 2100669–2100681 (2021).
22. Y. Liu *et al.*, *Adv. Energy Mater.* **10**, 2002539–2002548 (2020).
23. Y. Qi *et al.*, *Nat. Commun.* **13**, 484–492 (2022).
24. Y. Qi *et al.*, *Joule* **2**, 2393–2402 (2018).
25. Y. Wang *et al.*, *Adv. Energy Mater.* **11**, 2102452–2102460 (2021).
26. Z. Wang *et al.*, *Nat. Commun.* **12**, 1005–1013 (2021).
27. S. Guo *et al.*, *Adv. Funct. Mater.* **30**, 2003035–2003043 (2020).
28. Y. Liu *et al.*, *J. Mater. Chem. A Mater. Energy Sustain.* **10**, 19690–19698 (2022).
29. C. Bai *et al.*, *Nano Energy* **100**, 107449–107457 (2022).
30. C. Bai *et al.*, *ACS Appl. Mater. Interfaces* **13**, 37316–37322 (2021).
31. P. F. Salazar, S. T. Stephens, A. H. Kazim, J. M. Pringle, B. A. Cola, *J. Mater. Chem. A Mater. Energy Sustain.* **2**, 20676–20682 (2014).
32. Y. Yang *et al.*, *Proc. Natl. Acad. Sci. U.S.A.* **111**, 17011–17016 (2014).
33. T. J. Kang *et al.*, *Adv. Funct. Mater.* **22**, 477–489 (2012).
34. G. Li *et al.*, *Adv. Mater.* **31**, e1901403 (2019).
35. J. H. Kim, T. J. Kang, *ACS Appl. Mater. Interfaces* **11**, 28894–28899 (2019).
36. R. Hu *et al.*, *Nano Lett.* **10**, 838–846 (2010).
37. J. H. Lee, G. Shin, J. Y. Baek, T. J. Kang, *ACS Appl. Mater. Interfaces* **13**, 21157–21165 (2021).
38. L. Zhang *et al.*, *Adv. Mater.* **29**, 1605652–1605658 (2017).
39. C. Xu, Y. Sun, J. Zhang, W. Xu, H. Tian, *Adv. Energy Mater.* **12**, 2201542 (2022).
40. B. Yu *et al.*, *Nano Energy* **93**, 106795–106803 (2022).
41. D. Zhang *et al.*, *Energy Environ. Sci.* **15**, 2974–2982 (2022).
42. M. S. Romano *et al.*, *Adv. Mater.* **25**, 6602–6606 (2013).

ACKNOWLEDGMENTS

The authors thank the members of the Analytical & Testing Center of Northwestern Polytechnical University for their help with TEM characterization. **Funding:** X.L. acknowledges financial support from the National Natural Science Foundation of China (22261142666, 52172237); the Science, Technology, and Innovation Commission of Shenzhen Municipality (JCYJ008103417036); the Shaanxi Science Fund for Distinguished Young Scholars (2022JC-21); the Research Fund of the State Key Laboratory of Solidification Processing (NPU), China (grant no. 2021-QZ-02); and the Fundamental Research Funds for the Central Universities (3102019JC005). **Author contributions:** Conceptualization: X.L. and Y.W.; Methodology: X.L. and Y.W.; Investigation: X.L., Y.W., Y.Z., X.X., J.Y., M.W., R.W., P.G., and W.H.; Visualization: X.L. and Y.W.; Funding acquisition: X.L.; Project administration: X.L.; Supervision: X.L.; Writing – original draft: X.L., Y.W., A.J.S., and B.W.; Writing – review and editing: X.L., Y.W., A.J.S., and B.W. **Competing interests:** The authors declare that they have no competing interests, and have no patent applications or pending or awarded patents to declare. **Data and materials availability:** All data are available in the main text or the supplementary materials. **License information:** Copyright © 2023 the authors, some rights reserved; exclusive licensee American Association for the Advancement of Science. No claim to original US government works. <https://www.sciencemag.org/about/science-licenses-journal-article-reuse>

SUPPLEMENTARY MATERIALS

science.org/doi/10.1126/science.adg0164
Materials and Methods
Supplementary Text
Figs. S1 to S24
Notes S1 to S3
Tables S1 to S4
References (43–59).
Movie S1

Submitted 28 November 2022; resubmitted 15 March 2023
Accepted 16 May 2023
10.1126/science.adg0164



In situ photocatalytically enhanced thermogalvanic cells for electricity and hydrogen production

Yijin Wang, Youzi Zhang, Xu Xin, Jiabao Yang, Maohuai Wang, Ruiling Wang, Peng Guo, Wenjing Huang, Ana Jorge Sobrido, Bingqing Wei, and Xuanhua Li

Science, **381** (6655), .

DOI: 10.1126/science.adg0164

Editor's summary

In thermogalvanic cells, temperature-driven concentration gradients of redox-active species create a potential difference that can produce electricity. Wang *et al.* show that for the redox couple $\text{Fe}(\text{CN})_6^{4-}$ and $\text{Fe}(\text{CN})_6^{3-}$ in a gel matrix, water-splitting photocatalysts that generated oxygen and hydrogen boosted the concentration gradients of the redox ions and added a proton gradient to the cell (see the Perspective by Yu and Duan). The cell had a thermopower of 82 millivolts per degree kelvin and also generated a hydrogen by-product. —Phil Szuromi

View the article online

<https://www.science.org/doi/10.1126/science.adg0164>

Permissions

<https://www.science.org/help/reprints-and-permissions>

Use of this article is subject to the [Terms of service](#)

Science (ISSN) is published by the American Association for the Advancement of Science. 1200 New York Avenue NW, Washington, DC 20005. The title *Science* is a registered trademark of AAAS.

Copyright © 2023 The Authors, some rights reserved; exclusive licensee American Association for the Advancement of Science. No claim to original U.S. Government Works